The following publication L. Yang, M. Sun, M. Zhang and L. Zhang, "Multimodal Motion Control of Soft Ferrofluid Robot With Environment and Task Adaptability," in IEEE/ASME Transactions on Mechatronics, vol. 28, no. 6, pp. 3099-3109, Dec. 2023 is available at https://dx.doi.org/10.1109/TMECH.2023.3254663.

Multimodal Motion Control of Soft Ferrofluid Robot With Environment and Task Adaptability

Lidong Yang, *Member, IEEE*, Mengmeng Sun, *Member, IEEE*, Moqiu Zhang, *Student Member, IEEE*, and Li Zhang, *Fellow, IEEE*

***Abstract*—Soft microrobotics has recently been an active field that advances new microrobot design, adaptive motion and biomedical applications. In this work, we study the ferrofluid robot (FR), which has soft nature and exhibits paramagnetism. Currently, motion of the FR is usually realized by magnetic force, and the task execution requires relatively complex systems for simultaneous field and gradient control. To enable the FR with more motion modes for environment and task adaptability, we program three dynamic field forms and realize three corresponding torque-actuated motion modes: *Rolling*, *Wobbling*, and *Oscillating*. Together with the force-based *Dragging* mode, we provide a complete motion control scheme for the FR. As this scheme only requires 3D dynamic fields or gradients for actuation, the complexity of the magnetic actuation system is reduced. We formulate the motion and deformation actuation principles of the FR, and the four motion modes are demonstrated and characterized. With the implementation of automated tracking and control algorithms, controllability of the new torque-based modes is testified. We then fabricate different kinds of environments and cargoes to validate the environment and task adaptability of the FR by using the proposed scheme. Especially, we implement the scheme on a self-constructed system consisting of three mobile coils, and experiments realize the long-distance navigation of the FR via *Rolling* or *Dragging* modes. The ultrasound-guided navigation in a 3D tissue-mimicking endovascular environment shows the potential for delivery applications.**

***Index Terms*—Soft microrobot, ferrofluid, magnetic actuation, motion control.**

I. Introduction

UNTETHERED magnetic miniature robots have been used in various application scenarios due to their good accessibility to narrow regions and the penetration capability of magnetic fields [1], [2]. Their motion can also be well controlled to navigate in chip [3], [4], channel [5], and tubular [6], [7] environments by designing suitable motion modalities [8], [9]. Multimodal motion of non-deformable single [9] and swarm microrobots [10], [11] has further been proposed to improve their adaptability to environments. To provide corresponding programmed wireless magnetic actuation, magnetic actuation systems with various configurations have been designed [12]. With the development of magnetic microrobotic systems, potential *in-vivo* navigation has been realized for targeted delivery/therapy [13]–[15].

Traditional magnetic microrobots usually comprise rigid components, making them lack the flexibility to change their shape for environment adaption or lack the functionality enabled by morphology changing [16]. Recently, soft microrobots made of polymers, colloids, and gels have begun to reform the microrobot design [17], [18]. As a milestone, Fischer *et al.* proposed the elastomer-based mobile soft microrobots [19]. Driven by structure light-induced traveling waves, they can achieve translational and rotational motion. To develop magnetic field-responsive soft robots, the most common method utilizes gels with magnetic particles distributed inside [20]. Huang *et al.* fabricated bio-inspired hydrogel magnetic microswimmers and showed that the optimal swimming performance at different viscosities requires a specific swimmer configurations [21]. They can also adapt their shapes in response to mechanical constraints. Such hydrogel-based soft micromachines have been scaled down to microscale [22]. Lu *et al*. proposed the bio-inspired multilegged soft millirobot [23], [24], even with biodegradability [25]. Xu *et al.* realized the independent control of multiple polymer-based soft magnetic robots via differentiating their magnetization profiles [26]. In addition to the homogeneous materials, researchers proposed the configuration of multilink with different materials for soft microswimmers [27], [28]. To date, the development of diverse designs of soft microrobots not only shows the environment adaptability but also demonstrates higher levels of biodegradability and new multimodal motion mechanisms [29]. These properties make soft microrobots more capable of delivery to hard-to-reach regions inside human bodies [30].

Ferrofluid, a colloidal suspension of paramagnetic particles in a liquid medium, can respond to external magnetic fields with varying shapes and locations [31]. Recently, ferrofluid has been applied in a wide range of applications, such as microfluidics [32], cargo transportation [33], and biomedicine [34]. The super-soft nature of ferrofluid endows it with higher level of deformability such that the adaptive navigation in very constrained space becomes feasible, which is the limitation of the other types of soft microrobots. In addition, as liquid, ferrofluid can easily load drugs via injection, which is also an

This work was supported by the Innovation and Technology Fund (ITF) with Project No. MRP/036/18X, the Croucher Foundation grant with Ref. No. CAS20403, and the CUHK internal grants. The authors also thank the support from the SIAT-CUHK Joint Laboratory of Robotics and Intelligent Systems, and the Multi-scale Medical Robotics Center (MRC), InnoHK, at the Hong Kong Science Park. (*L. Yang and M. Sun contributed equally to this work*) (*Corresponding author: Li Zhang*)

L. Yang is with the Department of Industrial and Systems Engineering, The Hong Kong Polytechnic University, Kowloon, Hong Kong, China (e-mail: lidong.yang@polyu.edu.hk).

M. Sun, M. Zhang, and L. Zhang are with the Department of Mechanical and Automation Engineering, The Chinese University of Hong Kong (CUHK), Shatin NT, Hong Kong, China (e-mail: lizhang@mae.cuhk.edu.hk).

L. Zhang is also with the Department of Surgery, the Chow Yuk Ho Technology Centre for Innovative Medicine and CUHK T Stone Robotics Institute, The Chinese University of Hong Kong (CUHK), Shatin NT, Hong Kong, China.

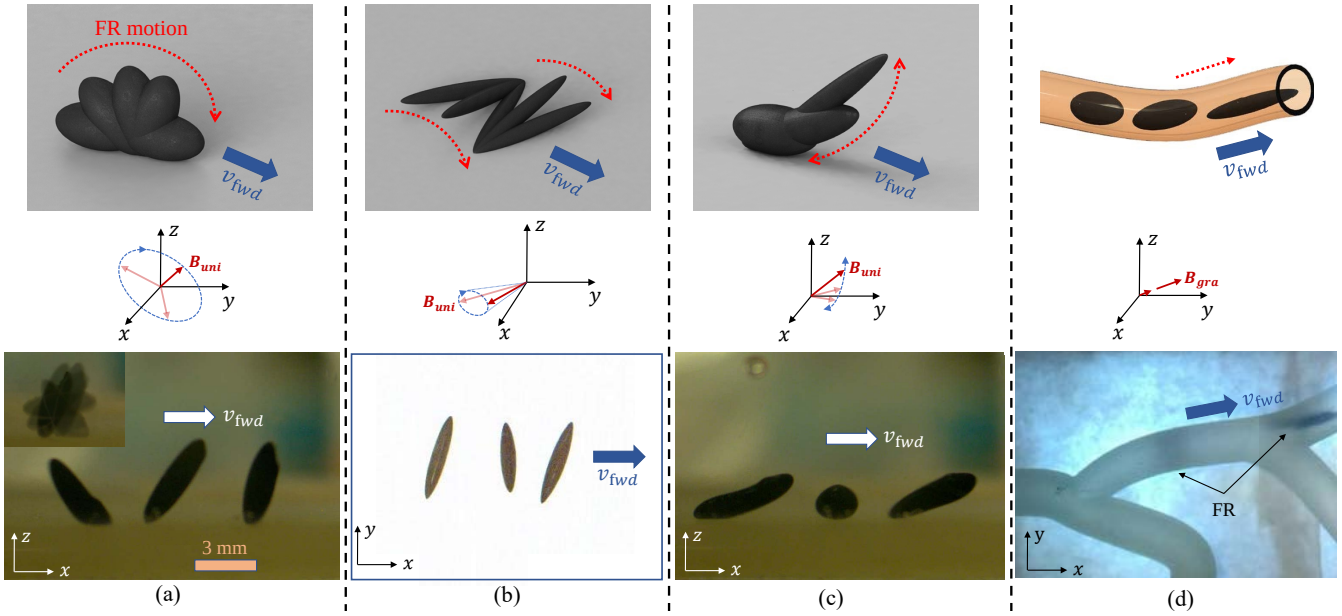

Fig. 1. Illustration of the four motion modes of the FR. The three rows show the schematics, the actuation magnetic fields, and the experimental illustrations, respectively. $\mathbf{v}_{\text{fwd}}$ denotes the forward motion vector. The scale bar applies for all the four experimental cases. In each case, an FR containing 20 μL ferrofluid is added into water for demonstration. (a) The *Rolling* motion. The inset shows the FR states in one cycle of the rolling motion. (b) The *Wobbling* motion. (c) The *Oscillating* motion. (d) The *Dragging* motion. Supplementary Video 1 includes the experimental illustrations of the four motion modes.

advantage for drug delivery applications.

In previous studies, motion of ferrofluid is usually actuated by magnetic forces. For example, the magnetic gradient can be controlled by a moving permanent magnet [35] and several electromagnetic coils [36]–[38]. A complex 2D coil array has further been used for parallel manipulation of multiple ferrofluid robots (FRs) [32], [33]. There is one issue associated with such force-based approaches. When performing cargo transport in open environments, the motion direction and the FR orientation are required to be simultaneously controlled, which requires a relatively complex magnetic actuation system to provide high control degree-of-freedom (Dof) [38], which may cause difficulty for applications. In addition, the fast decay of magnetic gradient (to the power of -4 with respect to the working distance) may also restrict the actuation efficiency for different kinds of working scenarios. Therefore, a multimodal motion control scheme of the FR requiring relatively simple magnetic actuation systems could reduce the application difficulty of the FR and enhance its adaptability to working environments or tasks.

In this work, we study the multimodal motion control of the FR, aiming to provide a complete motion control scheme for such soft robots. Compared with the conference version [39], we make additional contributions: 1) we model the mechanism of the FR deformation with experimental characterization; 2) we add a force-actuated mode to make the FR have the adaption in tubular environments; 3) we extend the multimodal control scheme to a mobile-coil system that can realize the large-workspace navigation using both torque and force-actuated modes, especially with ultrasound as the feedback.

The proposed scheme consists of four motion modes as illustrated in Fig. 1. Each of them has unique features suitable for specific environments or tasks. The *Rolling* mode (Fig. 1(a)) is actuated by rotating fields, and this type of motion is very common for microrobots working near a boundary [40], [41]. The *Wobbling* motion (Fig. 1(b)) is driven by conical fields. Under this mode, the FR moves along the direction of its short axis, which can be utilized for cargo transport via pushing actions. The *Oscillating* mode (Fig. 1(c)) is actuated by combined oscillating fields. Compared with the *Rolling* mode, the FR under this mode oscillates near the substrate so that it can pass through channels with confined roof structures. Forward motion of the three torque-based modes alleviates the fluidic force and the boundary interaction force. The *Dragging* mode is designed for navigating the FR in confined tubular environments, which thus purely relies on the magnetic force. As the four motion modes do not require the simultaneous field and gradient control, the proposed motion control scheme can be implemented on relatively simple magnetic actuation systems.

II. Magnetic Actuation Principles of The FR

A. Field-Induced Deformation

The hydrocarbon FR is purchased from Taobao (China), which has a dynamic viscosity of 50 Cp, a saturation magnetization of 34.3 kA/m, and a density of 1.29 g/ml. The weight fraction of Fe_3O_4 in the FR is 40%. For an FR surrounded by non-magnetizable liquid (e.g., water in this work), the magnetization induces a mismatch of the normal stress balance at the interface of the two liquids, and this stress mismatch forces the droplet to elongate along the field direction [42]. This field-induced deformation is derived as follows. When a linearly magnetizable ferrofluid in an isothermal system is

subject to a magnetic field $\mathbf{H}$, there would be a magnetic force at the ferrofluid-water interface [43] that can be computed by

$$\mathbf{F}_{\mathrm{m}} = -\frac{1}{2}H^2 \cdot \nabla\mu \tag{1}$$

where μ represents the magnetic permeability. To smooth the discontinuous fluid properties near the ferrofluid-water interface, a Heaviside function $H_\varepsilon(\phi)$ [44] is used that has the following expression:

$$H_\varepsilon(\phi) = \begin{cases} 0\ , & \text{if } \ \phi < -\varepsilon \\ \frac{1}{2}\left[1 + \frac{\phi}{\varepsilon} + \frac{1}{\pi}\sin\left(\frac{\pi\phi}{\varepsilon}\right)\right]\ , & \text{if } \ |\phi| \le \varepsilon \\ 1\ , & \text{if } \ \phi > \varepsilon \end{cases} \tag{2}$$

where ε is a tunable parameter referring to the thickness of the interface, and ϕ is a level set (LS) function which is negative in the ferrofluid, positive in the water and zero at the interface. Then the smoothed μ can be expressed as

$$\mu(\phi) = \mu_{\mathrm{W}} \cdot H_\varepsilon(\phi) + \mu_{\mathrm{F}} \cdot (1 - H_\varepsilon(\phi)) \tag{3}$$

where μ_{W} and μ_{F} denote the magnetic permeability of water and ferrofluid, respectively. Substitute Eq. (2) and (3) into Eq. (1), then we get

$$\mathbf{F}_{\mathrm{m}} = \begin{cases} 0\ , & \text{if } \ |\phi| > \varepsilon \\ -\frac{H^2(\mu_{\mathrm{W}} - \mu_{\mathrm{F}})}{2\varepsilon}\left[1 + \cos\left(\frac{\pi\phi}{\varepsilon}\right)\right]\nabla\phi\ , & \text{if } \ |\phi| \le \varepsilon \end{cases} \tag{4}$$

That is, $\mathbf{F}_{\mathrm{m}}$ only exists at the ferrofluid-water interface ($|\phi| \le \varepsilon$) and aligns with the negative gradient of ϕ. $\mathbf{F}_{\mathrm{m}}$ drives the FR to deform until the surface tension force $\mathbf{F}_{\mathrm{s}}$ counterbalance it. According to the Continuum Surface Force (CSF) model [45], $\mathbf{F}_{\mathrm{s}}$ can be calculated by

$$\begin{aligned} \mathbf{F}_{\mathrm{s}} &= \sigma\kappa\frac{\partial H_\varepsilon(\phi)}{\partial\phi}\nabla\phi \\ &= \begin{cases} 0\ , & \text{if } \ |\phi| > \varepsilon \\ \frac{\sigma\kappa}{2\varepsilon}\left[1 + \cos\left(\frac{\pi\phi}{\varepsilon}\right)\right]\nabla\phi\ , & \text{if } \ |\phi| \le \varepsilon \end{cases} \end{aligned} \tag{5}$$

where σ and κ are the surface tension coefficient and the curvature of the interface boundary, respectively. From Eq. (4) and (5), it can be obtained that a stronger magnetic field would induces a larger proportion of deformation. As $\mathbf{F}_{\mathrm{m}}$ is proportional to the square of the field strength, the growth rate of the surface curvature increases with the field strength, as validated by the characterization results in Fig. 2. After the deformation approaches saturation, the growth rate of the curvature then gradually decreases. Utilizing the actively controllable deformation, the FR can adapt to environments.

B. Torque-Based Motion Actuation

The torque actuation requires 3D dynamic fields that can be generated by simple magnetic manipulation systems. For example, we adopt a 3-axis Helmholtz coil system developed in Ref [28], whose 3D dynamic uniform field is denoted by $\mathbf{B}_{\mathrm{uni}}$. When subject to $\mathbf{B}_{\mathrm{uni}}$, the FR is magnetized, and the magnetic flux density inside the FR reads

$$\mathbf{B}_{\mathrm{F}} = \mathbf{B}_{\mathrm{uni}} + \mu_0 \cdot \mathbf{M}_{\mathrm{F}} \tag{6}$$

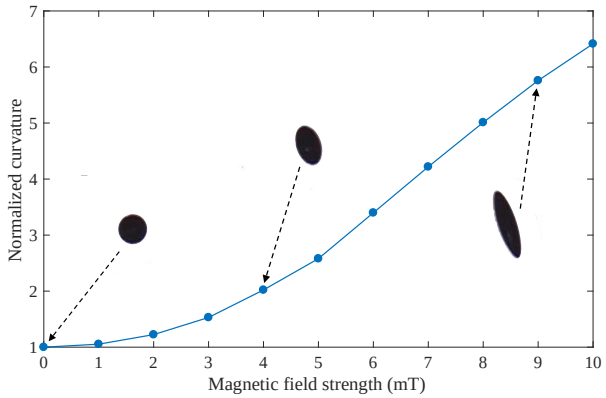

Fig. 2. Characterization results of the shape deformation. In the experiments, an FR contains 20 μL ferrofluid and is placed on a horizontal plate immersed in water. Each data point represents the average value of five measurements.

where $\mu_0 = 4\pi \times 10^{-7}$ N/A^2 is the magnetic vacuum permeability. $\mathbf{M}_{\mathrm{F}} = \chi\mathbf{H}_{\mathrm{uni}} = \chi\mathbf{B}_{\mathrm{uni}}/\mu_0$ denotes the magnetization of ferrofluid, in which χ is the susceptibility of ferrofluid. The magnetization direction aligns with the magnetic field lines, and the induced magnetic moment can be computed by

$$m_{\mathrm{F}} = \left[\coth(\lambda H_{\mathrm{uni}}) - \frac{1}{\lambda H_{\mathrm{uni}}}\right] V_{\mathrm{F}} M_{\mathrm{F}} \tag{7}$$

where V_{F} refers to the volume of the magnetic component, and $\lambda = \frac{3\chi}{M_{\mathrm{F}}}$. Besides the magnetization-induced deformation, with the magnetic moment, a dynamic magnetic filed would exert an magnetic torque on the FR, computed by

$$\tau = \mathbf{m}_{\mathrm{F}} \times \mathbf{B}_{\mathrm{uni}} \tag{8}$$

Thus, by suitably designing $\mathbf{B}_{\mathrm{uni}}$, the induced dynamic motion and deformation of the FR may generate controllable forward motion. Since torque-based motion modes mainly rely on fluidic effects, they are not desirable for FR navigating in constrained tubular environments.

C. Force-Based Motion Actuation

When placed in a magnetic gradient field $\mathbf{B}_{\mathrm{gra}}$, the FR would be subject to an external magnetic force:

$$\mathbf{F}_{\mathrm{mag}} = (\mathbf{m}_{\mathrm{F}} \cdot)\,\nabla\mathbf{B}_{\mathrm{gra}} \tag{9}$$

By controlling $\mathbf{B}_{\mathrm{gra}}$, forward motion of the FR can be easily generated via magnetic force, as illustrated by previous works [33], [38]. Considering that, when working in open space for task execution, the FR requires a complex magnetic actuation system to generate independently controllable field and gradient for simultaneous control of orientation and motion direction, we thus propose to apply the force-based motion only in tubular environments such that orientation of the FR is constrained and a system capable of generating 3D magnetic gradients is sufficient for actuation via magnetic force dragging.

III. Torque-Based Multimodal Motion Control

Previous works have well demonstrated the force-based motion, i.e., the *Dragging* mode, thus, in this section, we focus on studying the three torque-based motion modes.

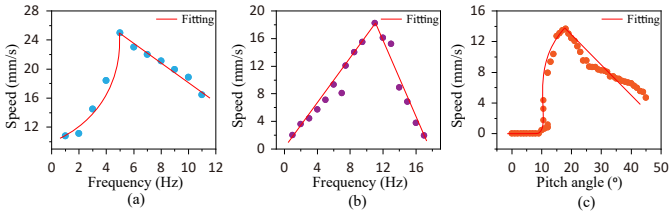

Fig. 3. Characterization results of the three torque-based motion modes. In all the experiments, 20 μL ferrofluid is added into a cuboid tank filled with water. (a) Results of the rolling motion with field strength 8 mT and pitch angle 90 °. (b) Results of the wobbling motion with field strength 8 mT and conical angle 15°. (c) Results of the oscillating motion with field strength 9 mT and frequency 10 Hz.

A. The Rolling Motion

The rolling motion is triggered by a rotating field expressed by

$$\begin{aligned}\mathbf{B}^{\mathrm{R}}_{\mathrm{uni}} &= \begin{bmatrix} \mathbf{B}^{\mathrm{R}}_{\mathrm{uni}}.x & \mathbf{B}^{\mathrm{R}}_{\mathrm{uni}}.y & \mathbf{B}^{\mathrm{R}}_{\mathrm{uni}}.z \end{bmatrix}^{\mathrm{T}} \\ &= \begin{bmatrix} B\left(\cos\beta\cos\alpha\cos(2\pi\omega t)+\sin\alpha\sin(2\pi\omega t)\right) \\ B\left(-\cos\beta\sin\alpha\cos(2\pi\omega t)+\cos\alpha\sin(2\pi\omega t)\right) \\ B\sin\beta\cos(2\pi\omega t) \end{bmatrix}\end{aligned} \tag{10}$$

where B, ω, β, α, and t represent the field strength, rotating frequency, pitch angle, yaw angle, and time, respectively. The magnetic torque induced by the field rotation makes the FR roll on the working surface, then the unbalanced fluidic force near and far from the surface and the friction force with the surface would drive the FR move forward. As shown in Fig. 1(a), the motion vector of the FR denoted by $\mathbf{v}_{\mathrm{fwd}}$ can be adjusted by controlling α and ω to change the motion direction and speed, respectively. The experimental illustration of this motion mode is included in the Supplementary Video 1. Characterization results of this motion are plotted in Fig. 2(a), where 20 μL ferrofluid is added into water and the field flux density is fixed at 8 mT. We can obtain that the motion speed increases with the field frequency for $\omega \leq 5$ Hz. Then, the FR enters the 'step-out' zone. It should be noted that an FR with a slender shape induced by a large field (e.g., 10 mT) may split at a high frequency (e.g., 20 Hz) due to the fluid drag force.

Utilizing this motion mode, the FR can navigate in open environments, and the elongation deformation can also enable it to move in narrow channel environments. If liquid cargo is injected to the FR [33], the *Rolling* mode could be used for delivery purposes.

B. The Wobbling Motion

The wobbling motion is actuated by a conical field expressed by

$$\mathbf{B}^{\mathrm{W}}_{\mathrm{uni}} = \begin{bmatrix} \mathbf{B}^{\mathrm{W}}_{\mathrm{uni}}.x & \mathbf{B}^{\mathrm{W}}_{\mathrm{uni}}.y & \mathbf{B}^{\mathrm{W}}_{\mathrm{uni}}.z \end{bmatrix}^{\mathrm{T}} \tag{11}$$

where

$$\begin{aligned}\mathbf{B}^{\mathrm{W}}_{\mathrm{uni}}.x =& B(\sin\eta\cos\beta\cos\alpha\cos(2\pi\omega t)+ \\ & \sin\eta\sin\alpha\sin(2\pi\omega t)+\cos\eta\sin\beta\cos\alpha) \end{aligned} \tag{12}$$

$$\begin{aligned}\mathbf{B}^{\mathrm{W}}_{\mathrm{uni}}.y =& B(\sin\eta\cos\beta\sin\alpha\cos(2\pi\omega t)- \\ & \sin\eta\cos\alpha\sin(2\pi\omega t)+\cos\eta\sin\beta\sin\alpha) \end{aligned} \tag{13}$$

$$\mathbf{B}^{\mathrm{W}}_{\mathrm{uni}}.z = -B(\sin\eta\sin\beta\cos(2\pi\omega t)+\cos\eta\cos\beta) \tag{14}$$

η denotes the conical angle, and the other symbols have the same meaning with those in Eq. (10). Regarding this motion mode, the motion direction and speed (shown in Fig. 1(b)) of the FR should be adjusted by controlling α and ω, respectively. Besides, increasing the conical angle η in a suitable region can also increase the motion speed. Characterization results of this motion are plotted in Fig. 3(b), where the field flux density and conical angle are fixed at 8 mT and 15°, respectively. It shows that the speed-frequency variation trend is similar to that of the rolling motion, but the different motion gait leads to slower speed but more stable forward motion.

As the FR always exhibits relatively long lengths in xy plane, the *Wobbling* mode can be used for cargo transport via the pushing action. However, also due to this specific property, the FR with this mode cannot pass through narrow channels and thus is only applicable for relatively open environments.

C. The Oscillating Motion

The oscillating motion is driven by a composite oscillating field $\mathbf{B}^{\mathrm{O}}_{\mathrm{uni}}$ generated by **Algorithm 1**. This field simultaneously regulates the shape deformation of the FR and its orientation oscillating in the vertical plane, as shown in Fig. 1(c). σ is the fraction between the FR elongation time and the vertical oscillating period. As shown in the Supplementary Movie S1, this composite oscillating motion of the soft FR would induce forward motion, leveraging the interaction with the surface and the fluidic resistance force.

Algorithm 1 Generation of the composite oscillating field for the *Oscillating* motion mode of the FR. $Mod(a, b)$ will return the remainder after division $\frac{a}{b}$.

Input: B, β, α, ω, σ, and t.
$t_1 = Mod(t, \frac{1}{\omega})$
if $t_1 \leq \frac{\sigma}{\omega}$ **then**
  $B_1 = B \cdot \sin(\frac{\pi}{2} \cdot \frac{\omega}{\sigma} \cdot t_1)$
  $\beta_1 = \beta \cdot \sin(\frac{\pi}{2} \cdot \frac{\omega}{\sigma} \cdot t_1)$
else
  $B_1 = B \cdot \sin(\frac{\pi}{2} \cdot \frac{\omega}{(1-\sigma)} \cdot t_1)$
  $\beta_1 = \beta \cdot \sin(\frac{\pi}{2} \cdot \frac{\omega}{(1-\sigma)} \cdot t_1)$
end if
$\mathbf{B}^{\mathrm{O}}_{\mathrm{uni}}.x = B_1 \cdot \cos\beta_1 \cos\alpha$
$\mathbf{B}^{\mathrm{O}}_{\mathrm{uni}}.y = B_1 \cdot \cos\beta_1 \sin\alpha$
$\mathbf{B}^{\mathrm{O}}_{\mathrm{uni}}.z = B_1 \cdot \sin\beta_1$
Output: $\mathbf{B}^{\mathrm{O}}_{\mathrm{uni}} = \begin{bmatrix} \mathbf{B}^{\mathrm{O}}_{\mathrm{uni}}.x & \mathbf{B}^{\mathrm{O}}_{\mathrm{uni}}.y & \mathbf{B}^{\mathrm{O}}_{\mathrm{uni}}.z \end{bmatrix}^{\mathrm{T}}$

The motion direction and speed are controlled by adjusting the field yaw angle ω and field pitch angle β, respectively. In the characterization experiments, we fix ω and σ as 10 Hz and 0.1, respectively, after careful tuning. The results in Fig.

3(c) indicate that the FR starts to move when β exceeds 10°, after which the motion speed also exhibits the increase-and-decrease behavior when the pitch angle β is gradually tuned up.

With this motion mode, the FR oscillates in the vertical plane so that it can navigate in both open environments and narrow channels. However, unlike the rolling motion that has large motion magnitudes in the vertical plane, the FR occupies much smaller space in the vertical direction, as shown in Fig. 1(a)(c). As a result, this mode can be applied to narrow channels even with roof structures, but the motion speed of this mode is slower than that of the *Rolling* mode. Regarding applications, the FR under this motion mode occupies relatively small vertical space, making it suitable for transport of lipophilic cargo that can be attached on the FR.

D. Automated Tracking and Motion Control

The ellipsoid shape of the FR makes its projections become ellipses. To track the FR, we adopt a statistics-based method [46] that uses 360 boundary points of the FR for ellipse fitting, and the center position $\mathbf{p}_{\mathrm{F}}$ is obtained. Results in Supporting Video 2 prove that the FR distribution can be well tracked in real time.

To testify the controllability of the multimodal motion of the FR, we implemented Proportional controllers for the automated motion control:

$$\begin{cases} u_x(t) = K_{\mathrm{P}} \left[\mathbf{p}_{\mathrm{F_d}}(t).x - \mathbf{p}_{\mathrm{F}}(t).x\right] \\ u_y(t) = K_{\mathrm{P}} \left[\mathbf{p}_{\mathrm{F_d}}(t).x - \mathbf{p}_{\mathrm{F}}(t).y\right] \end{cases} \tag{15}$$

where K_{P} is a positive control gain, and $\mathbf{p}_{\mathrm{F_d}}(t).x$ denotes the x component of the desired position at time instant t. Then, the field yaw angle is determined by

$$\alpha(t) = \arctan 2(u_y(t)/u_x(t)) \tag{16}$$

and the field parameter related to the speed control (i.e., the parameter of the x-axis in Fig. 3) is obtained by

$$u(t) = Sat(u_{\min}, \sqrt{u_x^2(t) + u_y^2(t)}, u_{\max}) \tag{17}$$

where the $Sat(\bullet)$ constrains the value of $\sqrt{u_x^2(t) + u_y^2(t)}$ to be within $(u_{\min}, u_{\max})$ if it exceeds this interval. $(u_{\min}, u_{\max})$ is chosen based on the characterization results so that it locates in the range within which the FR speed monotonically increases.

IV. Experimental Results

A. Automated Motion Control

The FR exhibits quasi-static states in the *Dragging* mode so that this motion can be well controlled [37], [38]. Herein, we aim to test the controllability of the three new torque-based motion modes.

1) Implementation on a Helmholtz Coil System: We implement the automated tracking and control method on a 3-axis Helmholtz coil system [28], inside which an open water tank contains an FR with 20 μL ferrofluid. After careful experimental parameter tuning, K_{P} is determined as 1.2, and $(u_{\min}, u_{\max})$ is set as $(0, 5)$ Hz, $(0, 10)$ Hz, and $(10°, 20°)$ for the *Rolling*, *Wobbling*, and *Oscillating* modes, respectively. Then, we conduct experiments to let the FR track a circular trajectory (diameter: 20 mm). Results illustrated in Fig. 4(a) validate that the *Rolling* and *Wobbling* modes exhibit steady controllable motion and both achieve high tracking accuracy, i.e., average error < 0.5 mm. For comparison, the *Oscillating* mode has unsteady motion caused by its simultaneously dynamic shape and orientation oscillations, resulting in failures for trajectory tracking tasks. We then reduce the difficulty of automated motion control for this mode: five target points are set to let the FR reach in sequence. Results in Fig. 3(b) show that, although the FR can reach the target point with controllability, it may circling around the target before the final reaching, showing weaker controllability than the other two torque-based modes. Detailed automated motion control processes are included in the Supplementary Video 2.

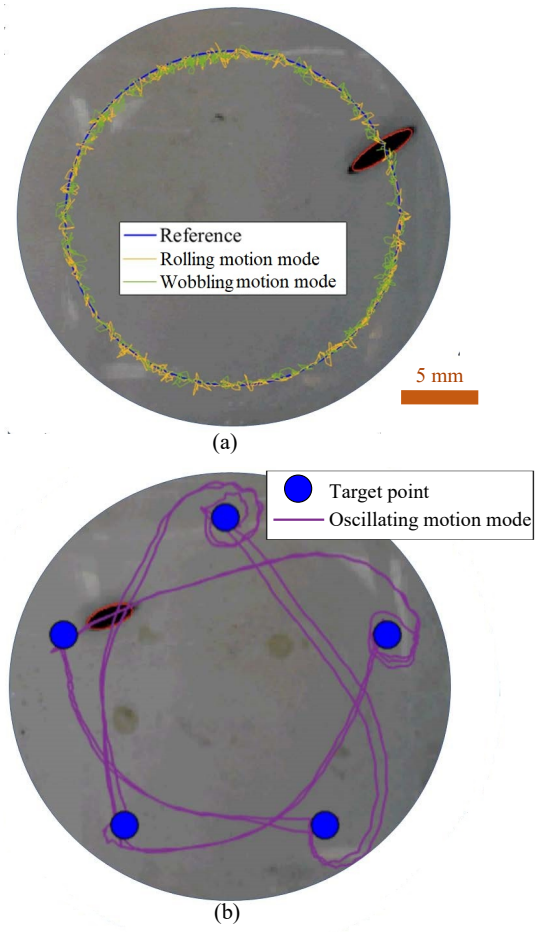

Fig. 4. Automated control results of the three torque-based motion modes, where the FR contains 20 μL ferrofluid. (a) With the *Rolling* and and *Wobbling* modes, the FR is controlled to track a circular trajectory. (b) With the *Oscillating* mode, the FR is controlled to reach five target points in sequence.

2) Implementation on a Mobile-Coil System: As the torque-based motion modes only require 3D dynamic fields, the motion control scheme can be implemented on magnetic actuation systems with three field control Dofs, e.g., the self-constructed system with three mobile coils [47] as illustrated in Fig. 5(a). The feedback camera is fixed on the so-called 'coil-end plate', and the moving space of the coil-end plate is

defined as the workspace of the system. This system has much larger workspace (Φ 500 mm) than the Helmholtz system that expands the navigation space of the FR. As shown in Fig. 5(b), the workspace can cover the entire human GI tract. In the entire workspace, it is evaluated that there are no singularities for both mechanical motion and field generation. We then transfer the automated tracking and control scheme to this system and conduct trajectory tracking experiments under the *Rolling* mode. Unlike the Helmholtz coil system that has uniform field in the entire workspace, the field of the mobile-coil system depends on the position of the FR and the poses of the three coils. To generate the field $\mathbf{B}(\mathbf{p}_\mathrm{F})$ output by the automated controller, the following equation based on the linear superposition law of magnetic fields is applied:

$$\mathbf{i} = \overline{\mathbf{H}}^{-1} \cdot \mathbf{B}(\mathbf{p}_\mathrm{F}) \tag{18}$$

where $\mathbf{i} = [i_1, i_2, i_3]^\mathrm{T}$ is the coil current vector. $\overline{\mathbf{H}} = \left[\bar{\mathbf{B}}_1(\mathbf{p}_\mathrm{F})\ \bar{\mathbf{B}}_2(\mathbf{p}_\mathrm{F})\ \bar{\mathbf{B}}_3(\mathbf{p}_\mathrm{F})\right]$ denotes the unit field vectors of the three coils at the FR position, whose detailed computation method can be found in Ref [47]. Based on the FR tracking result, Eq. (18) is executed in real time (50 Hz) to generate the demanded rotating field with a strength of 6 mT. Fig. 5(c) and Supplementary Video 3 show the automated tracking results of an ellipse trajectory (major axis: 200 mm). It is validated that the FR can also be well controlled by this system, and the average error is 1.89 mm. The control accuracy is lower than that using the Helmholtz system, which is mainly resulted from the non-zero magnetic gradient of the mobile-coil system.

B. Environment Adaptability

The automated control experiments show the controllable motion in open space. In this part, we fabricate environments with different kinds of constraints to show the environment adaptability of the FR by using the proposed multimodal motion control scheme.

1) Narrow Channel With Open Vertical Space: We first fabricate a channel environment via molding. The channel has a width of 2 mm and open vertical space. The *Rolling* and *Oscillating* modes are suitable for swift navigation in this type of environment, but the former one exhibit faster speed as indicated by the characterization results. As demonstrated in Fig. 6(a) and Supplementary Video 4, the FR with the rolling motion can easily pass through this environment with fast speed, if applying a relatively strong field (9 mT) to perform large elongation that avoids the FR being stuck in the narrow channel.

2) Narrow Channel With Constrained Vertical Space: Another type of channel environment we fabricate has roof structures to constrain the vertical space to 6 mm. The FR with *Rolling* mode cannot pass due to the large vertical space occupation. Thus, the *Oscillating* mode is the best motion mode for this environment. Fig. 6(b) validates that, using this motion mode, the FR can successfully pass through the vertically constrained channel and finally reach the target region. That is, although with relatively weaker controllability, the *Oscillating* mode has its unique navigation scenario.

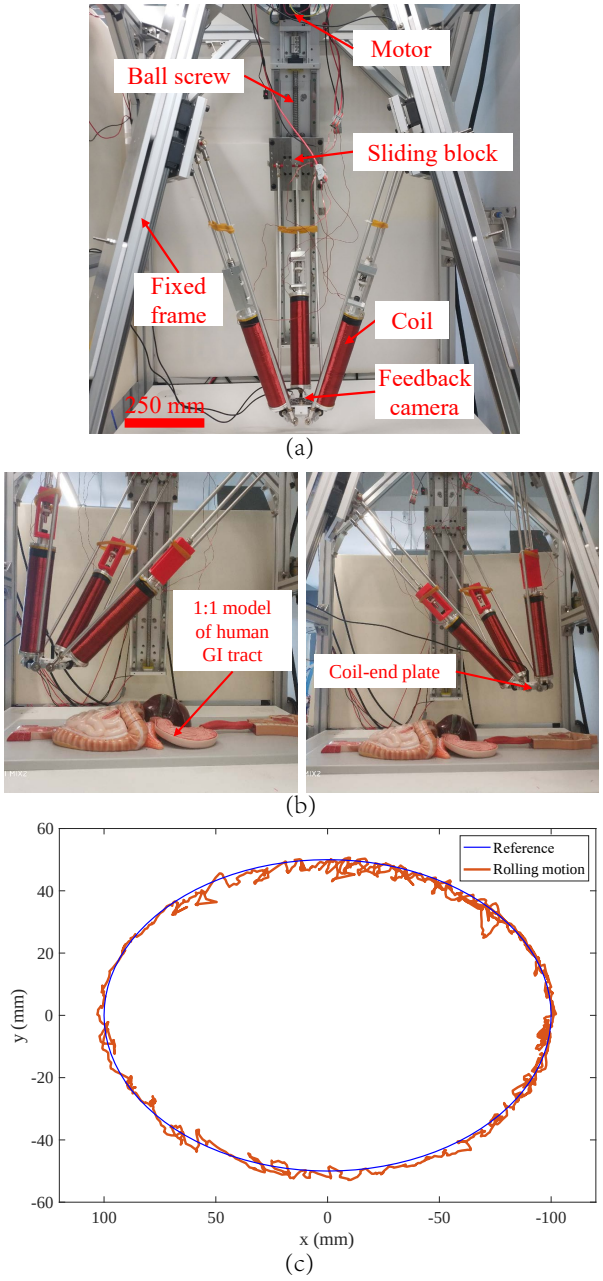

Fig. 5. Implementation of the automated tracking and control method on a self-constructed mobile-coil system. (a) A photo of the system. (b) Illustration of the system workspace, which can cover the entire human GI tract. (c) The trajectory tracking result for the *Rolling* mode, where the FR contains 20 μL ferrofluid. The experiment process is included in Supplementary Video 3.

3) Endovascular Environment: We also fabricate a 3D branched endovascular environment (inner diameter: 3 mm) via 3D printing, which is a common type of environment for microrobotic delivery. The soft nature of the FR enables it with the passive adaptability to such navigation cases, but the 3D gradient field control is also necessary to drive and guide the motion of the FR for active navigation. As 3D gradient control is sufficient, the self-constructed mobile-coil system is also capable for actuating this motion mode. Because the magnetic moment of the FR aligns with the magnetic field $\mathbf{B}(\mathbf{p}_\mathrm{F})$, the

following relation can be used for force computation:

$$\mathbf{m}_{\mathrm{F}} = ||\mathbf{m}_{\mathrm{F}}|| \cdot \bar{\mathbf{B}}(\mathbf{p}_{\mathrm{F}}) \tag{19}$$

where $\bar{\mathbf{B}}(\mathbf{p}_{\mathrm{F}})$ is the unit field vector at the FR position. Based on the linear superposition law, the magnetic force exerted on the FR can be calculated by

$$\mathbf{F}(\mathbf{p}_{\mathrm{F}}) = [\bar{\mathbf{G}}_1 \cdot \mathbf{m}_{\mathrm{F}},\ \bar{\mathbf{G}}_2 \cdot \mathbf{m}_{\mathrm{F}},\ \bar{\mathbf{G}}_3 \cdot \mathbf{m}_{\mathrm{F}}] \cdot \mathbf{i} \tag{20}$$

where $\bar{\mathbf{G}}_i$ denotes the unit field gradient matrix of the i-th coil at the position of the FR. Since, for a desired 3D force $\mathbf{F}_{\mathrm{d}}(\mathbf{p}_{\mathrm{F}})$, Eq. (19)(20) cannot be analytically solved to obtain the corresponding coil current vector $\mathbf{i}$, we propose an optimization method:

$$\begin{aligned} \min_{\mathbf{i}}\ & W_1 \cdot \left[-||\bar{\mathbf{F}}^{\mathrm{T}}(\mathbf{p}_{\mathrm{F}}) \cdot \bar{\mathbf{F}}_{\mathrm{d}}(\mathbf{p}_{\mathrm{F}})||\right] \\ & + W_2 \cdot ||\mathbf{F}(\mathbf{p}_{\mathrm{F}}) - \mathbf{F}_{\mathrm{d}}(\mathbf{p}_{\mathrm{F}})|| + ||\mathbf{i}|| \\ \text{subject to } & \begin{cases} \mathbf{i}_0 = [0,\ 0,\ 0]^{\mathrm{T}} \\ [\text{-}i_{\mathrm{bd}}\ \text{-}i_{\mathrm{bd}}\ \text{-}i_{\mathrm{bd}}]^{\mathrm{T}} \le \mathbf{i} \le [i_{\mathrm{bd}}\ i_{\mathrm{bd}}\ i_{\mathrm{bd}}]^{\mathrm{T}} \end{cases} \end{aligned} \tag{21}$$

where $\mathbf{i}_0$ is the initial value of $\mathbf{i}$, and $i_{\mathrm{bd}} = 10\mathrm{A}$ is the bound of coil current. The first and second terms in the cost function are to minimize the direction error and the magnitude error of the output magnetic force, respectively. The third term is to minimize the required coil currents. With careful experimental parameter tuning, constant weights W_1 and W_2 are set as 100 and 50, respectively. It is tested that solving this optimization problem requires tens of milliseconds using the *fmincon* function in Matlab, fulfilling the real-time use. By this method, the mobile-coil system can generate dynamic magnetic force for the *Dragging* motion mode. Fig. 6(c) demonstrates the navigation results in the 3D branched endovascular environment. The operator controls the magnetic force direction that successfully lead the FR to climb up the upper-right branch. Then, after switching off the field, the FR slides down due to the gravity force. Detailed navigation process is included in Supplementary Video 4.

C. Task Adaptability

Previous works have demonstrated the cargo transport by simultaneously controlling the orientation and motion of the FR using a eight-coil system [38] or an array of twenty-five coils [33]. Herein, we will show that the proposed multimodal motion control scheme can be used for transport of both lipophilic and hydrophilic cargoes, using relatively simple Helmholtz coil systems. Moreover, we also show that it is possible to use the system with three mobile coils to perform long-distance 3D endovascular delivery of the FR under guidance of ultrasound imaging.

1) Transport of a Lipophilic Cargo: As the FR contains an oil-based liquid medium, a lipophilic cargo can be attached to or immersed in the FR. Then, the *Rolling* or *Oscillating* modes can be adopted for fast transport in constrained environments. For the rolling motion, considering that the cargo would undergo up-and-down motion in the FR, the cargo transport may be unstable, and the FR may even split. Thus, the *Oscillating* mode with weak vertical motion is more suitable for this type of task. To transport the cargo, according to our experiments, the minimal diameter of the FR using this mode should be around 1.5 times of that of the cargo.

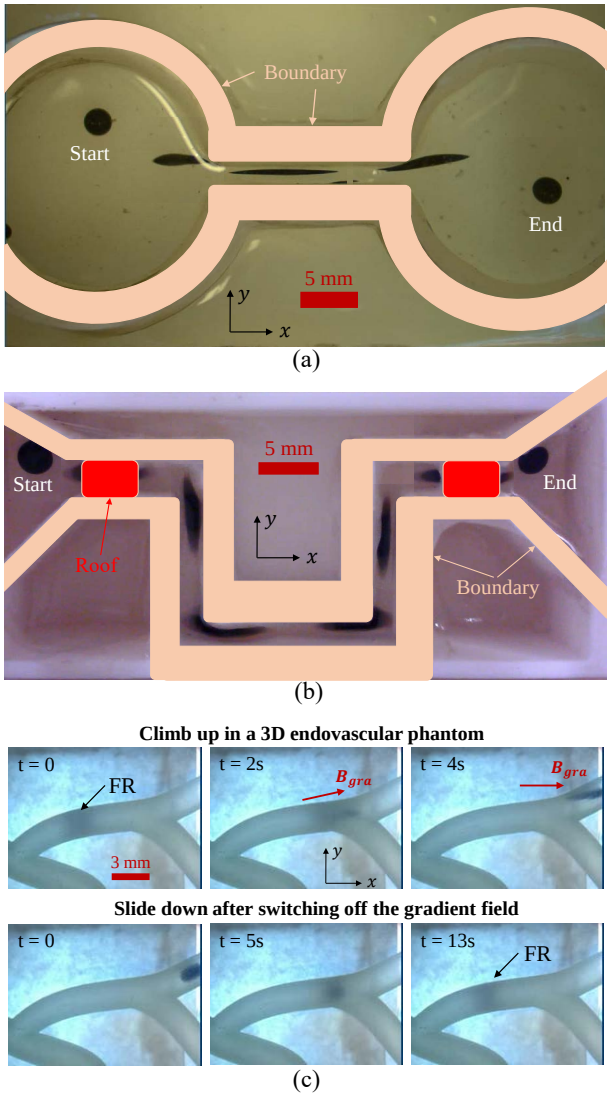

Fig. 6. Demonstrations of the environment adaptability of FR by using the proposed motion control scheme. (a) The *Rolling* mode is applied to a narrow channel environment with open vertical space. (b) The *Oscillating* mode is applied to a narrow channel environment with roof structures. (c) The *Dragging* mode is applied to a branched endovascular environment. Detailed experiment processes are included in Supplementary Video 4.

In this experiment, a 20 μL FR under the *Oscillating* mode is controlled to transport a sphere (diameter: 2 mm) made of EcoFlex from one side of the tank to the other by passing through a corridor. Fig. 7 and Supplementary Video 5 show the task execution process, which includes the cargo loading, cargo transport and cargo unloading procedures. With the controllable motion, the operator change the motion direction of the FR to make it approach the cargo, and the cargo is loaded when contacting with the FR. Then, the FR is controlled to transport the cargo. After reaching the targeted region, a 3D dynamic field programmed by Eq. (22) is applied to make the FR split by utilizing the repulsive magnetic forces of magnetic parts inside the FR, so that the cargo is released

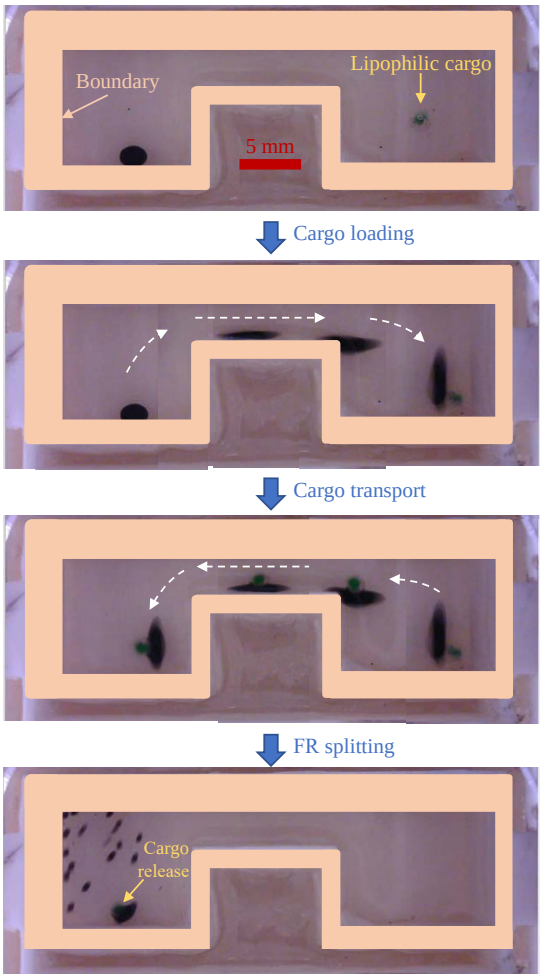

Fig. 7. Transport of a spherical lipophilic cargo made of EcoFlex, which has a diameter of 2 mm. The *Oscillating* motion mode is applied for this task.

from most of the ferrofluid.

$$\mathbf{B}^{\mathrm{S}}_{\mathrm{uni}} = \begin{bmatrix} \mathbf{B}^{\mathrm{S}}_{\mathrm{uni}}.x \\ \mathbf{B}^{\mathrm{S}}_{\mathrm{uni}}.y \\ \mathbf{B}^{\mathrm{S}}_{\mathrm{uni}}.z \end{bmatrix} = \begin{bmatrix} -B \cdot \sin(120 \cdot Ceil(5t)) \cdot \sin(2\pi\omega t) \\ B \cdot \cos(120 \cdot Ceil(5t)) \cdot \sin(2\pi\omega t) \\ B \cdot \cos(2\pi\omega t) \end{bmatrix} \quad (22)$$

The $Ceil(a)$ function in Eq. (22) outputs the closest integer not smaller than a, and the frequency ω is set as 15 Hz. After FR splitting control for cargo release, around 30% percent remains on the cargo. This value can be reduced by designing the cargo with a smaller portion of lipophilic surface.

2) Semi-Automated Transport of a Hydrophilic Cargo: As for hydrophilic cargoes, they cannot be attached to the FR for transport. Thus, the *Rolling* and *Oscillating* modes cannot be applied to this type of task. Considering that the *Wobbling* mode always makes the FR exhibit relatively long length in xy plane, this motion mode can transport the hydrophilic cargo via the pushing action. To smoothly pushing the cargo, according to our experiments, the minimal diameter of the FR using this mode should be around 2 times of that of the cargo.

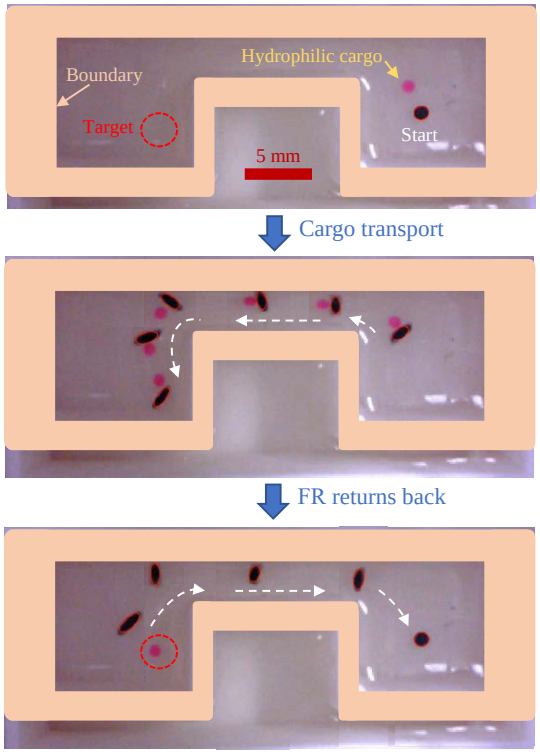

Fig. 8. Transport of a spherical hydrophilic cargo made of hydrogel, which has a diameter of 1 mm. The *Wobbling* motion mode is suitable for this task.

In the validation experiment, an FR containing 7 μL ferrofluid under the wobbling motion mode is used to transport a sphere (diameter: 1 mm) made of hydrogel from one side of the tank used in the previous task to the target region of the other side. To increase the autonomy level, we implement the automated tracking and motion control algorithms, and the operator only needs to select the target points that can lead the FR for the transport task. The task execution process is illustrated in Fig. 8 and Supplementary Video 6, showing that after every update of the target point selection, the FR automatically moves towards the target. Meanwhile, the cargo is pushed toward the final target region. After the transport task is completed, the target points are selected to lead the FR to return back to the other side of the tank.

3) Long-Distance Delivery of The FR under Ultrasound Guidance: Endovascular delivery under medical imaging is a common task for microrobots [48]. The FR is a potential candidate that can transport liquid cargo injected into it [33], [49]. However, the long-distance 3D endovascular navigation under guidance of medical imaging modalities has not been realized, which is the objective of this part. We adopt the mobile-coil system in Fig. 5(a), but the feedback camera is replaced by an ultrasound probe (Model: 16HL7,Terason Inc.) that can rotate about z axis to provide 3D feedback. A tissue-mimicking phantom with the recipe from Ref [50] is fabricated with a 3D endovascular structure (diameter: 3 mm) inside.

For this navigation experiment, we first perform the ultrasound scanning to locate the distribution of the endovascular structure, and then extract the its centerline. The tangent direction of the centerline is set as the desired magnetic

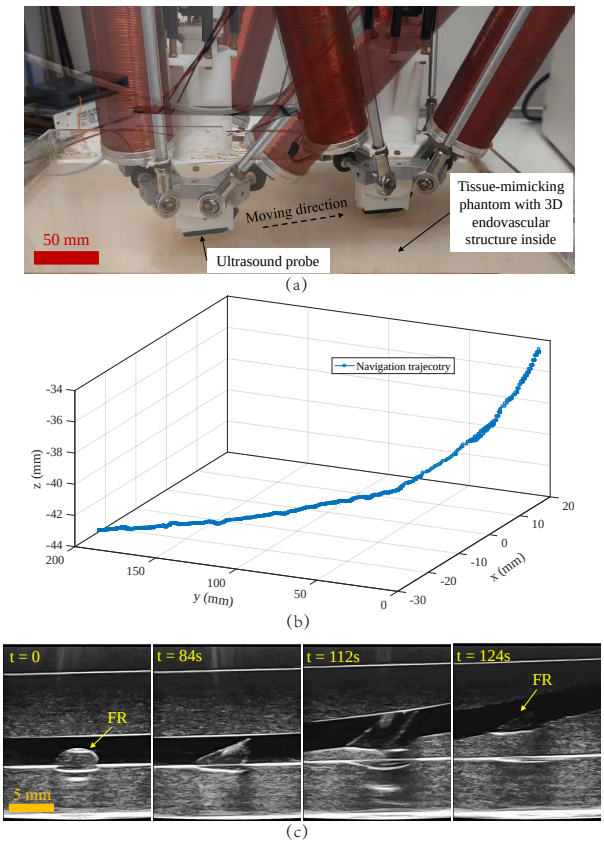

Fig. 9. Long-distance delivery of the FR under ultrasound imaging guidance. (a) The system setup. (b) The real-time navigation trajectory of the FR recorded in the experiment. (c) The ultrasound feedback images at four time instants.

force direction. During the navigation process, the imaging plane of the ultrasound probe is programmed to automatically align with the vertical tangent plane of the centerline of the endovascular structure. y coordinate of the probe is manually controlled to make the FR always within the imaging plane, and the desired magnetic force magnitude is adjusted to maintain steady navigation. Results in Supplementary Video 7 and Fig. 9 show that the system can move the ultrasound probe and adjust its orientation to track the FR during the long-distance navigation ($\sim$ 250 mm). Meanwhile, the system also generate the demanded force for actuating the FR in the 3D vascular structure. This experiment proves that the FR can be well tracked using ultrasound imaging. Meanwhile, we find that the ultrasound visibility of the FR decreases when the pitch angle of the navigation increases. The main reason is that the intersection angle between the ultrasound emitting direction and the ultrasound reflection direction increases. To avoid this issue, in the future, one more rotation Dof of the probe should be added to make such intersection angle as small as possible. When scaling the volume of an FR down to 1 mm^3, to overcome the net weight for smooth dragging motion, the required magnetic gradient is around 0.5 T/m with a magnetic field strength of 10 mT.

The three task demonstrations show that the FR can adapt to cargo transport and delivery tasks by suitably changing its motion mode.

V. Conclusion

In summary, we have presented a multimodal motion control scheme for the soft ferrofluid robot (FR) to enable it with capabilities to adapt to different environments or tasks. In the scheme, the *Rolling*, *Wobbling*, *Oscillating*, and *Dragging* motion modes are realized by programming four corresponding magnetic fields, which can be generated by relatively simple magnetic actuation systems with three control Dofs. Their motion properties are characterized, after which the automated control is implemented that validates the controllability of the three new torque-based motion modes via tracking experiments. Utilizing the scheme, we have also experimentally demonstrated the environment and task adaptability of the FR via switching its motion modes. Furthermore, we implement the proposed scheme on a self-constructed system with three mobile coils and demonstrate the long-distance navigation by torque or force-based motion modes. Especially, the ultrasound-guided navigation in tissue-mimicking phantom show the potential of FRs in delivery applications.

In the future, we intend to apply the proposed scheme to functionalized FR and explore its targeted therapy/delivery applications. Besides, we also plan to study the other medical imaging modalities-guided delivery of the FR, e.g., x-ray fluoroscopy.

References

[1] B. J. Nelson, I. K. Kaliakatsos, and J. J. Abbott, "Microrobots for minimally invasive medicine," *Ann. Rev. Biomed. Eng.*, vol. 12, pp. 55–85, 2010.

[2] M. Sitti and D. S. Wiersma, "Pros and cons: Magnetic versus optical microrobots," *Adv. Mater.*, vol. 32, no. 20, p. 1906766, 2020.

[3] S. Tasoglu, E. Diller, S. Guven, M. Sitti, and U. Demirci, "Untethered micro-robotic coding of three-dimensional material composition," *Nat. Commun.*, vol. 5, no. 1, pp. 1–9, 2014.

[4] S. Tottori, L. Zhang, F. Qiu, K. K. Krawczyk, A. Franco-Obregón, and B. J. Nelson, "Magnetic helical micromachines: fabrication, controlled swimming, and cargo transport," *Adv. Mater.*, vol. 24, no. 6, pp. 811–816, 2012.

[5] D. Folio and A. Ferreira, "Two-dimensional robust magnetic resonance navigation of a ferromagnetic microrobot using pareto optimality," *IEEE Trans. Robot.*, vol. 33, no. 3, pp. 583–593, 2017.

[6] J. Nam, W. Lee, J. Kim, and G. Jang, "Magnetic helical robot for targeted drug-delivery in tubular environments," *IEEE/ASME Trans. Mechatron.*, vol. 22, no. 6, pp. 2461–2468, 2017.

[7] K. Belharet, D. Folio, and A. Ferreira, "Endovascular navigation of a ferromagnetic microrobot using mri-based predictive control," in *2010 IEEE/RSJ Int. Conf. Intell. Robot. Syst.* IEEE, 2010, pp. 2804–2809.

[8] L. Yang and L. Zhang, "Motion control in magnetic microrobotics: From individual and multiple robots to swarms," *Annu. Rev. Control Robot. Auton. Syst.*, vol. 4, pp. 509–534, 2021.

[9] T. Xu, Z. Hao, C. Huang, J. Yu, L. Zhang, and X. Wu, "Multimodal locomotion control of needle-like microrobots assembled by ferromagnetic nanoparticles," *IEEE/ASME Trans. Mechatron.*, 2022.

[10] H. Xie, M. Sun, X. Fan, Z. Lin, W. Chen, L. Wang, L. Dong, and Q. He, "Reconfigurable magnetic microrobot swarm: Multimode transformation, locomotion, and manipulation," *Sci. Robot.*, vol. 4, no. 28, p. eaav8006, 2019.

[11] L. Yang, J. Jiang, X. Gao, Q. Wang, Q. Dou, and L. Zhang, "Autonomous environment-adaptive microrobot swarm navigation enabled by deep learning-based real-time distribution planning," *Nat. Mach. Intell.*, 2022, DOI=10.1038/s42256-022-00482-8.

[12] J. J. Abbott, E. Diller, and A. J. Petruska, "Magnetic methods in robotics," *Annu. Rev. Control Robot. Auton. Syst.*, vol. 3, pp. 57–90, 2020.

[13] J. Li, X. Li, T. Luo, R. Wang, C. Liu, S. Chen, D. Li, J. Yue, S.-h. Cheng, and D. Sun, "Development of a magnetic microrobot for carrying and delivering targeted cells," *Sci. Robot.*, vol. 3, no. 19, 2018.

[14] B. Wang, K. F. Chan, K. Yuan, Q. Wang, X. Xia, L. Yang, H. Ko, Y.-X. J. Wang, J. J. Y. Sung, P. W. Y. Chiu, *et al.*, "Endoscopy-assisted magnetic navigation of biohybrid soft microrobots with rapid endoluminal delivery and imaging," *Sci. Robot.*, vol. 6, no. 52, p. eabd2813, 2021.

[15] D. Li, D. Dong, W. Lam, L. Xing, T. Wei, and D. Sun, "Automated in vivo navigation of magnetic-driven microrobots using oct imaging feedback," *IEEE Trans. Biomed. Eng.*, vol. 67, no. 8, pp. 2349–2358, 2019.

[16] M. Sun, C. Tian, L. Mao, X. Meng, X. Shen, B. Hao, X. Wang, H. Xie, and L. Zhang, "Reconfigurable magnetic slime robot: Deformation, adaptability, and multifunction," *Adv. Funct. Mater.*, p. 2112508, 2022.

[17] C. Hu, S. Pané, and B. J. Nelson, "Soft micro-and nanorobotics," *Annu. Rev. Control Robot. Auton. Syst.*, vol. 1, pp. 53–75, 2018.

[18] J. Zhang and E. Diller, "Untethered miniature soft robots: Modeling and design of a millimeter-scale swimming magnetic sheet," *Soft Robot.*, vol. 5, no. 6, pp. 761–776, 2018.

[19] S. Palagi, A. G. Mark, S. Y. Reigh, K. Melde, T. Qiu, H. Zeng, C. Parmeggiani, D. Martella, A. Sanchez-Castillo, N. Kapernaum, *et al.*, "Structured light enables biomimetic swimming and versatile locomotion of photoresponsive soft microrobots," *Nat. Mater.*, vol. 15, no. 6, pp. 647–653, 2016.

[20] T. Xu, J. Zhang, M. Salehizadeh, O. Onaizah, and E. Diller, "Millimeter-scale flexible robots with programmable three-dimensional magnetization and motions," *Sci. Robot.*, vol. 4, no. 29, p. eaav4494, 2019.

[21] H.-W. Huang, F. E. Uslu, P. Katsamba, E. Lauga, M. S. Sakar, and B. J. Nelson, "Adaptive locomotion of artificial microswimmers," *Sci. Adv.*, vol. 5, no. 1, p. eaau1532, 2019.

[22] T.-Y. Huang, H.-W. Huang, D. Jin, Q. Chen, J. Huang, L. Zhang, and H. Duan, "Four-dimensional micro-building blocks," *Sci. Adv.*, vol. 6, no. 3, p. eaav8219, 2020.

[23] H. Lu, M. Zhang, Y. Yang, Q. Huang, T. Fukuda, Z. Wang, and Y. Shen, "A bioinspired multilegged soft millirobot that functions in both dry and wet conditions," *Nat. Commun.*, vol. 9, no. 1, pp. 1–7, 2018.

[24] H. Lu, Y. Hong, Y. Yang, Z. Yang, and Y. Shen, "Battery-less soft millirobot that can move, sense, and communicate remotely by coupling the magnetic and piezoelectric effects," *Adv. Sci.*, vol. 7, no. 13, p. 2000069, 2020.

[25] R. Tan, X. Yang, H. Lu, L. Yang, T. Zhang, J. Miao, Y. Feng, and Y. Shen, "Nanofiber-based biodegradable millirobot with controllable anchoring and adaptive stepwise release functions," *Matter*, vol. 5, no. 4, pp. 1277–1295, 2022.

[26] T. Xu, C. Huang, Z. Lai, and X. Wu, "Independent control strategy of multiple magnetic flexible millirobots for position control and path following," *IEEE Trans. Robot.*, vol. 38, no. 5, pp. 2875–2887, 2022.

[27] B. Jang, E. Gutman, N. Stucki, B. F. Seitz, P. D. Wendel-García, T. Newton, J. Pokki, O. Ergeneman, S. Pané, Y. Or, *et al.*, "Undulatory locomotion of magnetic multilink nanoswimmers," *Nano Lett.*, vol. 15, no. 7, pp. 4829–4833, 2015.

[28] L. Yang, Q. Wang, C.-I. Vong, and L. Zhang, "A miniature flexible-link magnetic swimming robot with two vibration modes: design, modeling and characterization," *IEEE Robot. Autom. Lett.*, vol. 2, no. 4, pp. 2024–2031, 2017.

[29] W. Hu, G. Z. Lum, M. Mastrangeli, and M. Sitti, "Small-scale soft-bodied robot with multimodal locomotion," *Nature*, vol. 554, no. 7690, pp. 81–85, 2018.

[30] H.-W. Huang, M. W. Tibbitt, T.-Y. Huang, and B. J. Nelson, "Matryoshka-inspired micro-origami capsules to enhance loading, encapsulation, and transport of drugs," *Soft Robot.*, vol. 6, no. 1, pp. 150–159, 2019.

[31] K. Raj, B. Moskowitz, and R. Casciari, "Advances in ferrofluid technology," *J. Magn. Magn. Mater.*, vol. 149, no. 1-2, pp. 174–180, 1995.

[32] W. Yu, H. Lin, Y. Wang, X. He, N. Chen, K. Sun, D. Lo, B. Cheng, C. Yeung, J. Tan, *et al.*, "A ferrobotic system for automated microfluidic logistics," *Sci. Robot.*, vol. 5, no. 39, p. eaba4411, 2020.

[33] X. Fan, X. Dong, A. C. Karacakol, H. Xie, and M. Sitti, "Reconfigurable multifunctional ferrofluid droplet robots," *Proc. Natl. Acad. Sci.*, vol. 117, no. 45, pp. 27 916–27 926, 2020.

[34] X. Zhang, L. Sun, Y. Yu, and Y. Zhao, "Flexible ferrofluids: Design and applications," *Adv. Mater.*, vol. 31, no. 51, p. 1903497, 2019.

[35] K. Zhang, Q. Liang, X. Ai, P. Hu, Y. Wang, and G. Luo, "On-demand microfluidic droplet manipulation using hydrophobic ferrofluid as a continuous-phase," *Lab Chip*, vol. 11, no. 7, pp. 1271–1275, 2011.

[36] M. A. Bijarchi, A. Favakeh, E. Sedighi, and M. B. Shafii, "Ferrofluid droplet manipulation using an adjustable alternating magnetic field," *Sens. Actuator A Phys.*, vol. 301, p. 111753, 2020.

[37] F. Kong, Y. Zhu, C. Yang, H. Jin, J. Zhao, and H. Cai, "Integrated locomotion and deformation of a magnetic soft robot: Modeling, control, and experiments," *IEEE Trans. Indus. Electron.*, vol. 68, no. 6, pp. 5078–5087, 2020.

[38] R. Ahmed, M. Ilami, J. Bant, B. Beigzadeh, and H. Marvi, "A shapeshifting ferrofluidic robot," *Soft Robot.*, 2020.

[39] L. Yang, M. Sun, and L. Zhang, "Torque-actuated multimodal locomotion of ferrofluid robot with environment and task adaptability," in *2022 IEEE/RSJ Int. Conf. Intell. Robot. Syst. (IROS)*. IEEE, 2022, pp. 2542–2547.

[40] R. Pieters, H.-W. Tung, S. Charreyron, D. F. Sargent, and B. J. Nelson, "Rodbot: A rolling microrobot for micromanipulation," in *2015 IEEE Int. Conf. Robot. Autom. (ICRA)*. IEEE, 2015, pp. 4042–4047.

[41] Y. Zhang, L. Zhang, L. Yang, C. I. Vong, K. F. Chan, W. K. Wu, T. N. Kwong, N. W. Lo, M. Ip, S. H. Wong, *et al.*, "Real-time tracking of fluorescent magnetic spore–based microrobots for remote detection of c. diff toxins," *Sci. Adv.*, vol. 5, no. 1, p. eaau9650, 2019.

[42] G.-P. Zhu, N.-T. Nguyen, R. V. Ramanujan, and X.-Y. Huang, "Nonlinear deformation of a ferrofluid droplet in a uniform magnetic field," *Langmuir*, vol. 27, no. 24, pp. 14 834–14 841, 2011.

[43] R. E. Rosensweig, *Ferrohydrodynamics*. Courier Corporation, 2013.

[44] M. Sussman, E. Fatemi, P. Smereka, and S. Osher, "An improved level set method for incompressible two-phase flows," *Computers & Fluids*, vol. 27, no. 5-6, pp. 663–680, 1998.

[45] J. U. Brackbill, D. B. Kothe, and C. Zemach, "A continuum method for modeling surface tension," *J. Comput. Phys.*, vol. 100, no. 2, pp. 335–354, 1992.

[46] L. Yang, J. Yu, and L. Zhang, "Statistics-based automated control for a swarm of paramagnetic nanoparticles in 2-d space," *IEEE Trans. Robot.*, vol. 36, no. 1, pp. 254–270, 2019.

[47] Z. Yang, L. Yang, and L. Zhang, "Autonomous navigation of magnetic microrobots in a large workspace using mobile-coil system," *IEEE/ASME Trans. Mechatron.*, vol. 26, no. 6, pp. 3163–3174, 2021.

[48] S. Pane, V. Iacovacci, E. Sinibaldi, and A. Menciassi, "Real-time imaging and tracking of microrobots in tissues using ultrasound phase analysis," *Appl. Phys. Lett.*, vol. 118, no. 1, p. 014102, 2021.

[49] Y. Ji, C. Gan, Y. Dai, X. Bai, Z. Zhu, L. Song, L. Wang, H. Chen, J. Zhong, and L. Feng, "Deformable ferrofluid microrobot with omnidirectional self-adaptive mobility," *J. Appl. Phys.*, vol. 131, no. 6, p. 064701, 2022.

[50] J. R. Cook, R. R. Bouchard, and S. Y. Emelianov, "Tissue-mimicking phantoms for photoacoustic and ultrasonic imaging," *Biomed. Opt. Express*, vol. 2, no. 11, pp. 3193–3206, 2011.

Lidong Yang (M'20) received the B.Eng. degree in mechanical design, fabrication, and automation from the Harbin Institute of Technology, Harbin, China, in 2014, and the Ph.D. degree in mechanical and automation engineering from The Chinese University of Hong Kong (CUHK), Hong Kong, in 2020.

He worked as a Postdoctoral Fellow with CUHK from 2020 to 2022. He is currently an Assistant Professor with The Hong Kong Polytechnic University (PolyU), Hong Kong. His research interests include the development and control of electromagnetic systems, microrobotics, and medical robotics at small scales.

Dr. Yang received the 2021 Excellent Doctoral Dissertation Nomination Award from Chinese Association of Automation (CAA), 2022 Young Scientist Finalist Award from Hong Kong Institution of Science, and Best Student Paper Award at the 2020 IEEE International Conference on Automation Science and Engineering.

Mengmeng Sun (M'21) received the bachelorâs degree in mechanical design, fabrication, and automation from the Wuhan University, Wuhan, China, in 2016, and the Ph.D. degree in mechanical and automation engineering from the Harbin Institute of Technology, Harbin, China, in 2021.

He is currently a Postdoctoral Fellow with the Department of Mechanical and Automation Engineering, The Chinese University of Hong Kong. His research interests include collective behaviors of micro/nanorobots, soft miniature robots, and medical imaging-guided active delivery for biomedical applications.

Moqiu Zhang (S'20) received his bachelor degree in petroleum engineering from the China University of Petroleum, East China, in 2014, and the master degree in mechanical and automation engineering from The Chinese University of Hong Kong, Hong Kong, in 2019. He is currently working toward the Ph.D. degree with the Department of Mechanical and Automation Engineering, The Chinese University of Hong Kong.

His research interests include magnetic manipulation system development, magnetic localization, and robotic control algorithm.

Li Zhang (Fellow'22) received the Ph.D.degree in physics from the University of Basel, Basel, Switzerland, in 2007.

He was a Postdoctoral Fellow and a Senior Scientist with the Institute of Robotics and Intelligent Systems (IRIS), Swiss Federal Institute of Technology (ETH), Zurich, Switzerland, from 2007 to 2012. He is currently a Professor with the Department of Mechanical and Automation Engineering, The Chinese University of Hong Kong, Hong Kong. His main research interests include microrobotics and nanorobotics for biomedical applications and their collective behaviors for the development of intelligent robot swarms at small scales.

Dr. Zhang received the Hong Kong Research Grants Council (RGC) Early Career Award in 2013, RGC Research Fellow Award in 2021, and several awards from IEEE conferences, including ICRA, IROS, CASE, ARM, NANOMED and 3M-NANO. He is also a Distinguished Lecturer appointed by the IEEE Nanotechnology Council (IEEE NTC) twice.